Vortex evolution in the near wake behind polygonal cylinders

Qingyang Wang[1,2], Lian Gan[3],†, Shengjin Xu[1],† and Yu Zhou[4]

[1]AML, School of Aerospace Engineering, Tsinghua University, 100084, China

[2]China Automotive Engineering Research Institute Co., Ltd., Chongqing, 401122, China

[3]Department of Engineering, Durham University, DH1 3LE, UK

[4]Institute for Turbulence-Noise-Vibration Interaction and Control, Harbin Institute of Technology (Shenzhen), 518050, China

†Corresponding author. E-mails: lian.gan@durham.ac.uk; xu_shengjin@tsinghua.edu.cn

The near wake of the polygonal cylinder with the side number $N = 3 \sim \infty$ is systematically studied using particle image velocimetry (PIV) at $Re = 1.6 \times 10^4$. The proper orthogonal decomposition (POD) analysis is carried out to extract the large-scale coherent vortex structures and their evolution. It has been found that the vortex circulation grows to the maximum at the vortex formation length by entraining the vorticity from the separated shear layer and then undergoes a two-stage decay. The maximum circulation scales with the wake width, defined as the vertical distance between the two peaks of streamwise velocity fluctuation at vortex formation length. The vortex center trajectory indicates that the vortices move towards the centerline first and then away, with the vortex size monotonically increasing over the examined streamwise range. The vortex size at the maximum circulation also scales with the wake width. The vortex convection velocity increases gradually in the streamwise direction, and the ratio of the lateral and streamwise components of the vortex convection velocity, when scaled by wake width and vortex formation length respectively, approaches asymptotically 0.18 in the downstream, irrespective of the cylinder orientation or N.

Keywords: polygonal cylinder; near wake; vortex street evolution

1. Introduction

Polygonal cylinders have many engineering applications, such as in fluid machineries, nuclear power generation systems, architecture and ocean engineering (Szalay 1989; Tang *et al*. 2013). Polygonal cylinders with different side number N can manifest very different characteristics in flow separation, vortex formation and vortex convection in the wake, which may cause dramatic changes to the fluid forces acting on the cylinders (Apelt *et al*. 1973; Chopra & Mittal 2019) and the stability of their wake (Monkewitz & Nguyen 1987; Unal & Rockwell 1988). Thus, it is important to understand the vortex shedding mechanism and their evolution in the wake behind polygonal cylinders with different side numbers.

While the studies of the wake behind the circular cylinder ($N = \infty$) amount to hundreds in the literature, investigations on the polygonal cylinder wake are rather scattered. The square cylinder ($N = 4$) wake (e.g. Lyn *et al*. 1995; Vickery 1966; Zhou & Antonia 1994) has attracted more attention than other polygonal cylinders ($4 < N < \infty$). Zhou & Antonia (1994, 1995) compared the wakes of triangular ($N = 3$), square ($N = 4$) and circular ($N = \infty$) cylinders and noted that, given the same Reynolds number (Re), the square cylinder produced larger velocity deficit, Reynolds stresses and vorticity magnitudes than that of the triangular and circular cylinders. Further, the Strouhal number (St) was different from one cylinder to another. Agrwal, Dutta & Gandhi (2016) discussed the effect of the apex angle of a triangular cylinder on the wake and found that the size of the reverse flow zone depended on the flow separation angle at the separation point, which was very much determined by the apex angle. Khaledi & Andersson (2011) investigated numerically the near wake of a hexagonal cylinder for both corner and face orientations at $Re = 100$, 500 and 1000. They found that St was generally higher for the face orientation than the corner. The St increased from $Re = 100$ to 500 but not anymore from $Re = 500$ to 1000, irrespective of the orientation. Kim *et al*. (2015) studied experimentally the wind-induced vibration on the straight and helical super-tall buildings of various polygonal sections of $N = 3 \sim 6$, 8, 12 and ∞. They found that vibration was gradually suppressed as N becomes larger. The helical cylinders were found to vibrate less than the straight cylinders. However, the difference diminished between the two types for $N > 5$.

Xu *et al.* (2017) systematically studied aerodynamic forces on the polygonal cylinders of $N = 2 \sim 8$, 12, 16, along with $N = \infty$. They established the dependence of drag coefficient C_D, *St* and the flow separation angle on *N*, and found that C_D and *St* scaled with a corrected separation angle ξ. However, in the above mentioned studies, the characteristics of the wake and vortex evolution behind those polygonal cylinders and their dependence on *N* were not systematically investigated.

In this work, we aim to experimentally study the vortex street evolution behind the polygonal cylinders and its dependence on side number *N* using particle image velocimetry (PIV) at subcritical regime, $Re = 1.6 \times 10^4$. Most of the researches to date on the cylinder wake are conducted over this subcritical regime, because of the relatively stable vortex shedding behavior (Bearman 1969; Lin *et al.* 1995; Norberg 2003; Pereira 2019). The proper orthogonal decomposition (POD) technique is deployed to extract the coherent motions from the PIV data. Experimental details are given in Section 2. Statistical quantities in the wake of polygonal cylinder are presented in Section 3.1. The wake POD analysis is conducted in Section 3.2. Coherent vortex structures and their evolution obtained from the POD analysis are shown in Section 3.3, followed by the discussion and conclusions in Section 4.

2. Experimental details

Experiments were carried out in an open-circuit low-speed wind tunnel with a square working section of 0.5m×0.5m×2.0m. The flow speed U_∞ within the test section ranges from 2m/s to 40m/s and the streamwise turbulence intensity is less than 0.5% for the current experimental velocity. The polygonal cylinder was supported horizontally in the symmetry plane of the working section, as shown in figure 1(a) where a square cylinder was installed. Two end plates were attached at the ends of the cylinder in order to suppress the end effect. Figure 1(b) shows the test models of polygonal cylinders with side number $N = 3 \sim 8$, 12, 16 and a circular cylinder ($N = \infty$). Measurements were conducted for two orientations of each polygonal cylinder, corner orientation or face orientation (see figure 1b for notations and abbreviations). In order to obtain the same *Re* at the same U_∞ and the same blockage ratio for all cylinders, two sets of cylinder models were designed for the

polygons of even *N* to ensure projected cylinder width *D* = 25mm for both corner and face orientations. The blockage of all polygonal cylinders is 5%. The cylinder length *L* between the two end plates was 420mm, giving an aspect ratio *L/D* = 16.8, at which the blockage as well as the three-dimensional end effect can be negligible. The Reynolds number, *Re* = $U_\infty D/v$, is set at 1.6×10^4, where *v* is the kinematic viscosity of air, corresponding to the subcritical regime of the polygonal cylinder (Xu *et al.* 2017).

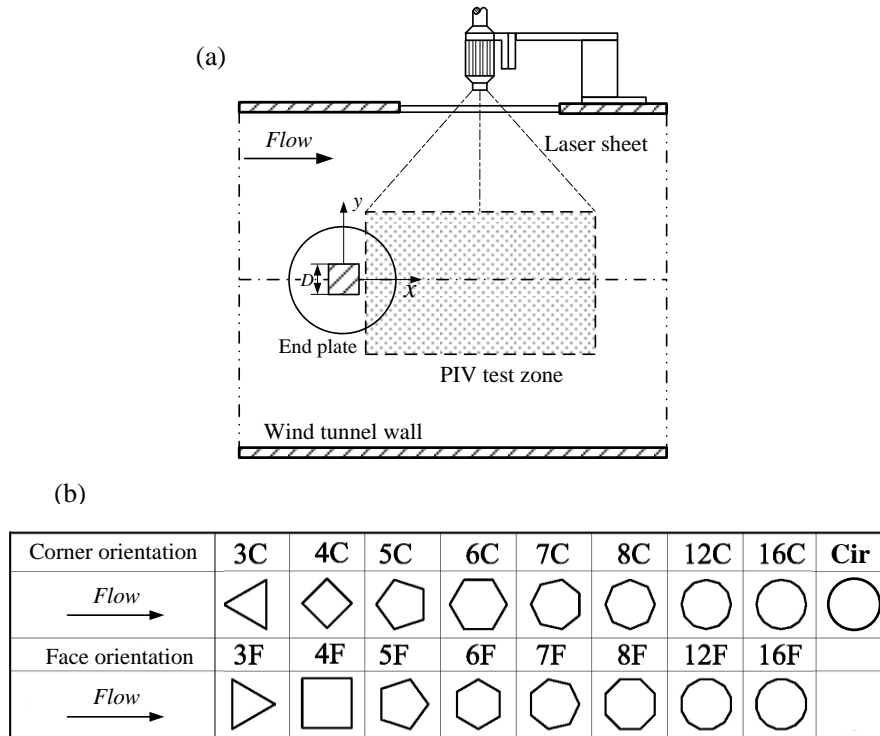| Corner orientation	3C	4C	5C	6C	7C	8C	12C	16C	Cir
Flow →	◁	◇	⬠	⬡	⬡	⬡	○	○	○
Face orientation	3F	4F	5F	6F	7F	8F	12F	16F	
Flow →	▷	□	⬠	⬡	○	○	○	○	

FIGURE 1. Experimental setup (not to scale), (a) one example of the test model, (b) the notations and abbreviations for the test models.

The flow field behind the cylinder was measured using a standard LaVision planar PIV system. Flow illumination was provided by a double-pulsed Nd-YAG Laser source with a wavelength of 532nm and a maximum energy output of 120mJ per pulse. A high sensitivity Imager Pro X CCD camera with a resolution of 2048 pixels $\times$ 2048 pixels was deployed to capture the particle images. The PIV Δt was set at 85μs. Flow was seeded with smoke particles of about 1 μm in diameter, generated from paraffin oil via Laskin nozzles.

The origin of the coordinate system is set at the center of the polygonal cylinder (figure 1a). The field of view (FOV) was fixed at 0.7 $\lesssim x/D \lesssim$ 8.0 and -2.0 $\lesssim y/D \lesssim$

2.0. The PIV sampling rate was 4 Hz. The sample size for each testing case was 1000, which had been verified to reach a good convergence for all the statistical quantities examined in the present study. A careful assessment of the St values reported previously in Xu $et\ al.$ (2017), measured at the same Re, indicates that the present sampling rate has no phase-locking issues for all the testing cases. That is, sufficiently random samples were acquired at all phases of the vortex shedding cycle. The raw PIV images were processed using DaVis 7.2, with a final interrogation window (IW) size of 32×32 pixels and 50% overlap, resulting in a spatial resolution of 1.85 mm based on the IW size.

3.   Results and discussion

3.1. *Statistical characteristics*

Distributions of the time mean velocity and Reynolds stresses fields in the polygonal cylinder wake are studied in this section. First, we introduce two parameters to facilitate the analysis and discussion. The vortex formation length L_f^* is defined as the streamwise position where the root mean square (RMS) value u'_{rms} of the fluctuating streamwise velocity u' on the wake centerline reaches the maxima (Bloor 1964; Alam, Zhou & Wang 2011). The wake width D_w^* is defined to be the lateral separation between the two u'_{rms} peaks at $x^* = L_f^*$ (Griffin 1995). In this paper, asterisk denotes normalizations by cylinder characteristic width D. These two length parameters are often used to characterize the wake size behind a two dimensional bluff body, and are obtained from the streamwise component of the Reynolds normal stresses.
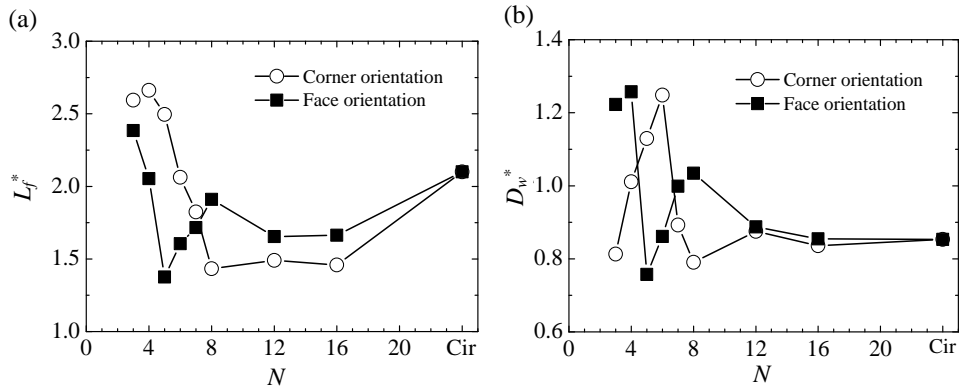

FIGURE 2. Dependence on N of the vortex formation length L_f^* and the wake width D_w^* at $Re = 1.6 \times 10^4$.

The dependence of L_f^* and D_w^* on N and orientation is presented in figure 2. It shows that the corner and face orientations exhibit very different behaviors for $N \leq 8$. For corner

cases, L_f^* displays a small rise and then a large monotonic drop to the minimum at $N = 8$. Whilst for face cases, L_f^* drops initially until $N = 5$ and then rises above the corner cases, reaching its peak at $N = 8$. For $N > 8$, L_f^* approaches a constant about 1.5 for corner orientation and 1.7 for face orientation approximately, and then gradually increase to the circular cylinder case at 2.1. On the other hand, D_w^* is a strong increasing function of N for $3 \le N \le 6$ of the corner cases, but after reaching the peak at $N = 6$, it declines quickly to the minimum value at $N = 8$. For face cases, D_w^* reflects a large drop from the maximum value at $N = 4$ to the minimum at $N = 5$ and then rises till $N = 8$. For $N > 8$, D_w^* also gradually approaches a constant about 0.85. Overall, 8C and 5F cases have the smallest L_f^* and D_w^* for corner and face orientations.
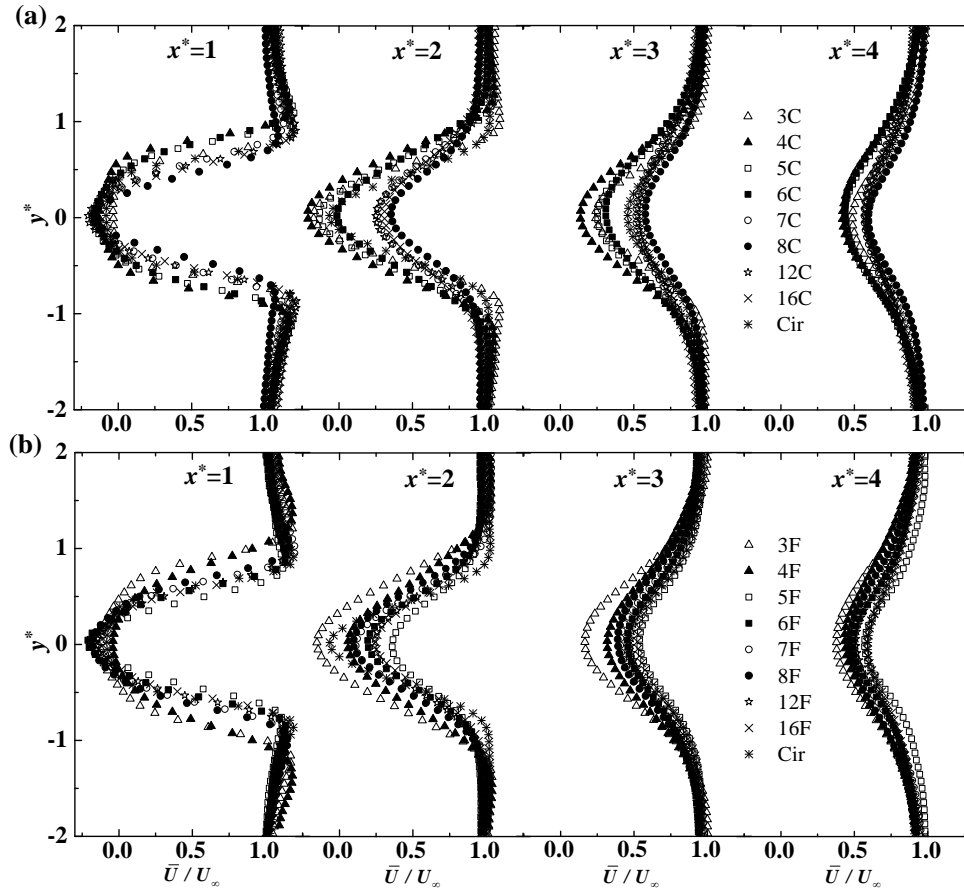

FIGURE 3. Mean streamwise velocity profiles along the transverse direction at different downstream distances for different polygonal cylinders, (a) corner orientation; (b) face orientation.

Figure 3 presents the time mean streamwise velocity $\bar{U}$ profiles at various downstream locations. As expected, the maximum velocity deficit deceases gradually with increasing x^*. Given the same projection height D, the velocity deficit of 4C is laterally

largest at $x^* = 1$ of the corner facing cases and that of 8C is smallest (figure 3a), it stems from the different separation point locations for the two cases and is in consistence with the transverse distance from the vortex centroid to the wake centerline. In addition, 8C shows the fastest velocity recovery in the streamwise direction, which is attributed to the relatively small vortex strength of this case (see section 3.3). The face orientation cases show similar patterns; see figure 3(b). The width of velocity deficit is largest for 3F and smallest for 5F. The latter also corresponds to the fastest velocity recovery. That is, at $Re = 1.6 \times 10^4$, 8C and 5F are characterized by the smallest wake width, which is consistent with figure 2(b). It will be shown later that the two cases correspond to the smallest distance between the upper and lower vortex center trajectories and also the weakest vortex strength.
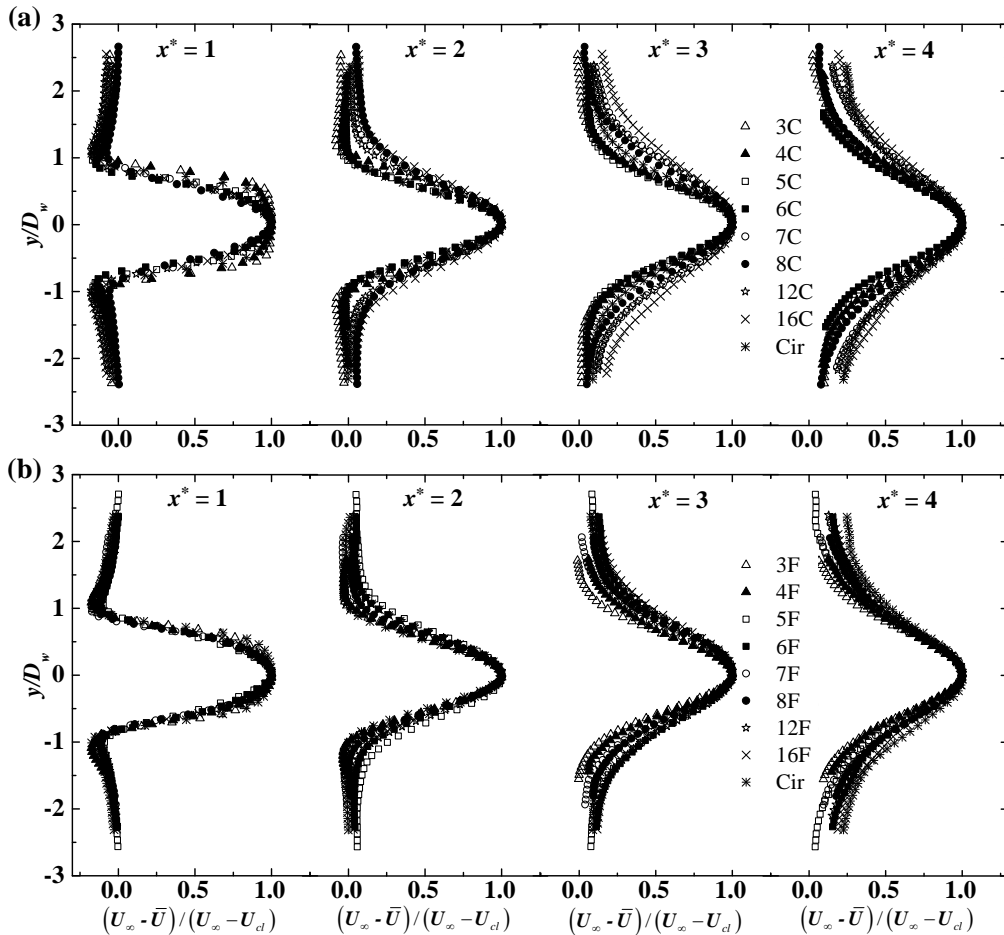

FIGURE 4. Non-dimensional mean velocity deficit profiles based on the wake width D_w, (a) corner orientation; (b) face orientation.

The normalised mean velocity deficit based on the wake width D_w is shown in Figure 4, where U_{cl} being the mean streamwise velocity on the wake centerline. It can be seen that the profiles collapse reasonably well especially for $x \leq 2D$. Further downstream, Wygnanski, Champagne & Marasli (1986) suggests that the momentum defect Θ is an important characteristic length scale in a small-deficit wake, i.e., the far wake. The momentum defect Θ is defined as

$$\Theta = \int_{-2D}^{2D} \frac{\bar{U}}{U_\infty}\left(1 - \frac{\bar{U}}{U_\infty}\right)dy. \tag{1}$$

The Θ normalised velocity deficit is presented in Figure 5 for $x \geq 3D$. It is evident that Θ is indeed a suitable length scale for the far field wake width and is independent of the polygonal cylinder side number N. Closer to the cylinders, the premise of small-deficit wake breaks and therefore the normalisation fails to work.

Figures 4 and 5 thus suggest that D_w works well for the near wake with large velocity deficit where $x \leq L_f$, whilst Θ is a better scaling parameter for $x \gg L_f$.
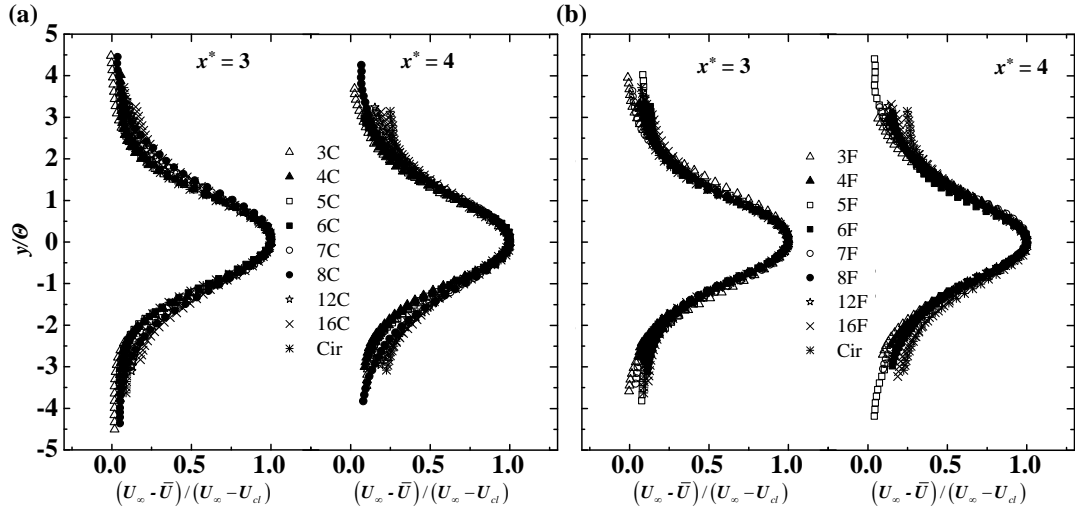

FIGURE 5. Non-dimensional mean velocity deficit profiles based on the momentum defect Θ, (a) corner orientation; (b) face orientation.
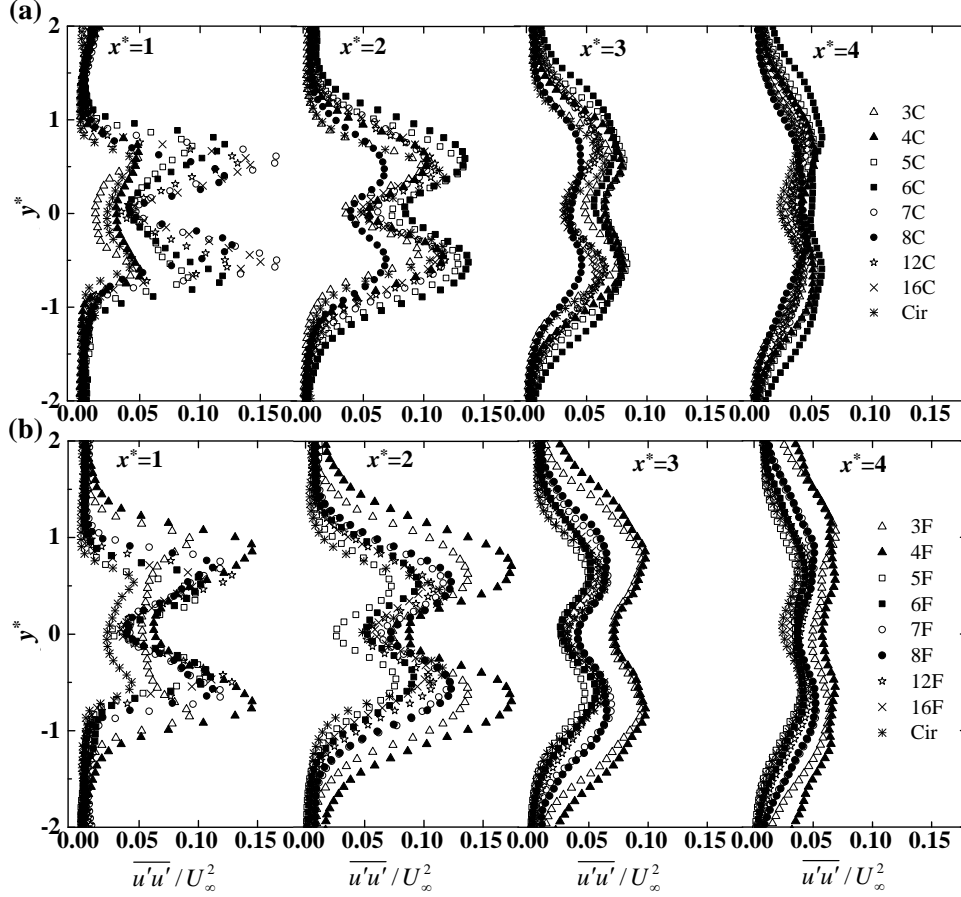
FIGURE 6. Profiles of the streamwise Reynolds normal stress $\overline{u'u'}/U_\infty^2$ for different polygonal cylinders, (a) the corner orientation; (b) the face orientation.

The streamwise Reynolds normal stress $\overline{u'u'}$ profiles are presented for different polygonal cylinders in figure 6. The profiles display a twin-peak pattern in the near wake, reflecting shear layers associated with vortices separated from the upper and lower surfaces of the cylinders (He, Li & Wang 2014). The rapidly growing peaks at $x^* < 2$ indicates the enhanced velocity fluctuation during the separated shear layer rollup process. For the corner orientation cases (figure 6a), the two peaks in $\overline{u'u'}$ exhibit the largest lateral distance in case 6C. The maximum $\overline{u'u'}$ magnitude of 6C is about $0.14 U_0^2$ at $x^* = 2$, but the lateral distance between the two peaks is the smallest at this x location. For the face orientation (figure 6b), case 4F has the strongest $\overline{u'u'}$. The streamwise variation of $\overline{u'u'}$ shows its maximum value at $x^* = 1$ for 8C and 5F, resulting in the smallest L_f^* of all. This is consistent with figure 2(a).
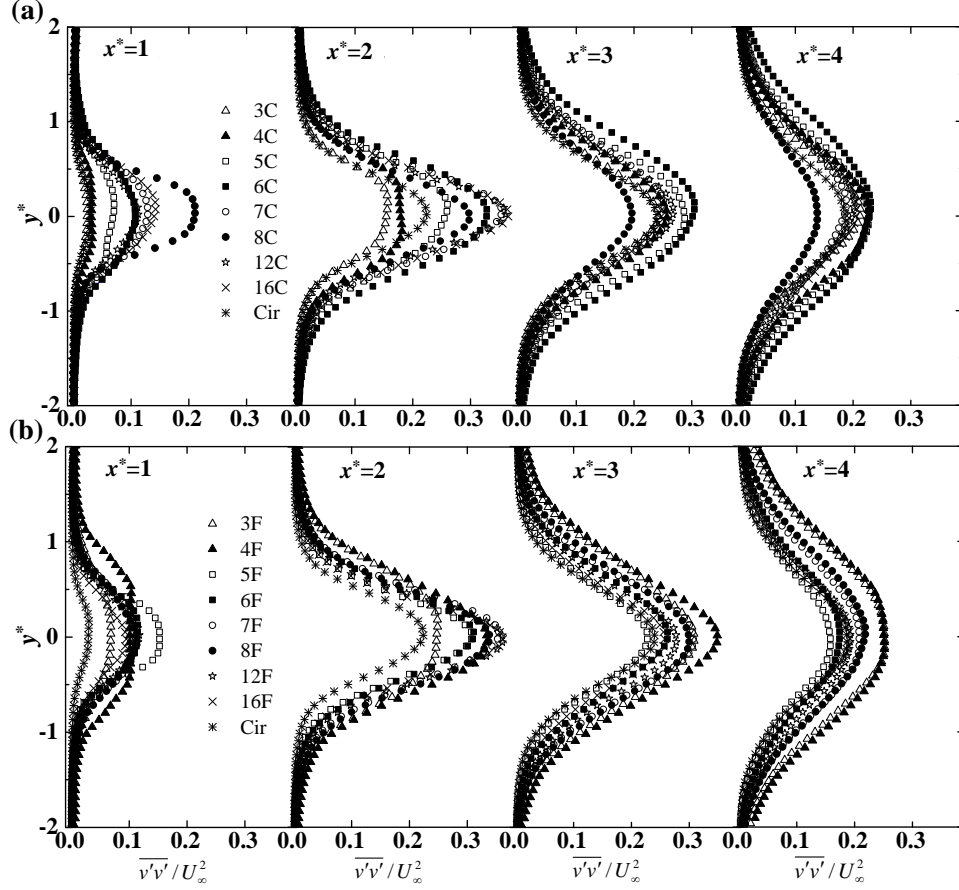
FIGURE 7. Profiles of the Reynolds normal stress $\overline{v'v'}/U_\infty^2$ for different polygonal cylinders, (a) the corner orientation; (b) the face orientation.

The profiles of the Reynolds normal stress $\overline{v'v'}$ (figure 7) display a single-peak distribution. The lateral width of the $\overline{v'v'}$ profile is in general correlated with the lateral distance between the oppositely signed vortex rows separated from the upper and lower cylinder surface. The peak in $\overline{v'v'}$, corresponding to the strongest interactions between the two vortex rows, reaches the maximum value between $x^* = 2$ and $x^* = 3$ in general. After that, the maximum $\overline{v'v'}/U_\infty^2$ retreats with increasing x^*, due to a decay of the vortex strength. Evidently, 6C and 4F case have the largest $\overline{v'v'}$ magnitude for the corner and face orientations, respectively, which agrees with the observation in $\overline{u'u'}$ behaviour. On the contrary, 8C and 5F are associated with the smallest $\overline{v'v'}$ for $x^* > 2$.
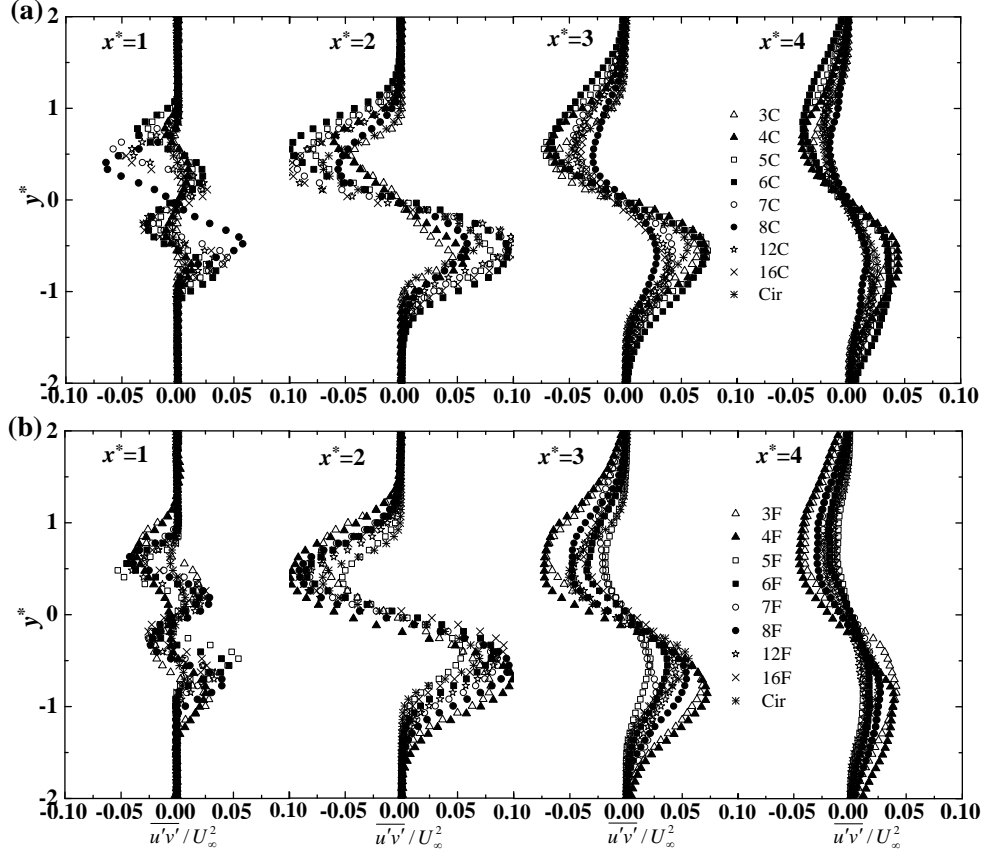
10

FIGURE 8. Profiles of the Reynolds shear stress $\overline{u'v'}/U_\infty^2$ for different polygonal cylinders, (a) corner orientation; (b) face orientation.

Figure 8 presents the Reynolds shear stress $\overline{u'v'}/U_\infty^2$. The peak and valley located around the upper and lower shear layers, move away from the centerline and the magnitude decreases with the increase of streamwise distance. In consistent with figure 6, 6C and 4F cases have the highest $\overline{u'v'}/U_\infty^2$ magnitude and the widest distribution in y direction ($x^* > 1$), corresponding to the widest wake width D_w^* (figure 2b). On the other hand, 8C and 5F cases have the lowest magnitude and narrowest the distribution, in line with the shortest vortex formation length L_f^* and wake width D_w^*.

3.2. *POD analysis*

In this section, flow field reduced order reconstruction using the snapshot-based POD technique (Sirovich 1987; Meyer, Pedersen & Ozcan 2007) is deployed to extract the coherent vortex street structures to better understand the observations made above. Recently, POD method has been successfully applied for extracting the coherent structures in turbulent wakes, jets and channel flows (e.g. Feng *et al.* 2011; Kaffel et al. 2016;

Muralidhar 2019; Qu *et al*. 2017). It has also been used to reconstruct the lower order flow structures to reflect the dominant flow dynamics with the least number of modes (Bai *et al*. 2019; Shi & Feng 2015; Tang *et al*. 2015).

Due to the quasi-two dimensional nature of the flow field, the information captured by the current experimental arrangement is a good reflection of the true total energy content in the flow, which is then decomposed into orthogonal modes via POD. Constructing an auto covariance matrix M,

$$M = U^T U, \tag{2}$$

where $U = [u_1, u_2 \dots u_{N_s}]$, with subscripts N_s representing the total snapshot number and u the instantaneous velocity vectors in each snapshot reorganized into a single column, a standard eigenvalue problem is solved

$$M A_i = \lambda_i A_i, \tag{3}$$

to obtain the eigenvalue λ_i, which represents the energy content in mode i and the eigenvector A_i. The associated POD mode i can be calculated as

$$\phi_i = \frac{\sum_{n=1}^{N_s} A_{i,n} u_n}{\left\| \sum_{n=1}^{N_s} A_{i,n} u_n \right\|}, \quad i = 1, 2, ..., N_s, \tag{4}$$

Sorting the eigenvalue λ_i in descending order ranks the energy level contained in the corresponding POD mode ϕ_i. Then the first few modes having higher energy content can be used to reconstruct the flow field containing only the coherent components; the higher order modes (with higher λ_i ranks) have lower energy level and represent incoherent structures or noise. For a detailed mathematical discussions about POD, readers are referred to Sirovich (1987); Berkooz, Holmes & Lumley (1993); Chatterjee (2000).

Note that using the instantaneous velocity u or the fluctuating velocity u' to construct M leads to similar results (Meyer, Pedersen & Ozcan 2007). If u' is used, the reconstruction of the instantaneous flow field can be written as equation (5), otherwise, the mean velocity term $U(x)$ will be taken into account in the summation term.

$$u(x) = U(x) + u'(x) = U(x) + \sum_{n=1}^{N_s} a_n \phi_n(x), \tag{5}$$

where $\phi_n(x)$ is obtained from equation (4), n being the order number of the POD mode.

The POD coefficient a_n is obtained by projecting the velocity field (either the fluctuating part as shown in equation 5 or the instantaneous) onto the POD modes, i.e.

$$a_n = \begin{bmatrix} \phi_1 & \phi_2 & ... & \phi_{N_s} \end{bmatrix}^T u_n, \tag{6}$$

Reduced order reconstruction of instantaneous fields is realized by taking $n < N_s$ in equation (5), depending on the desired proportion of energy content.
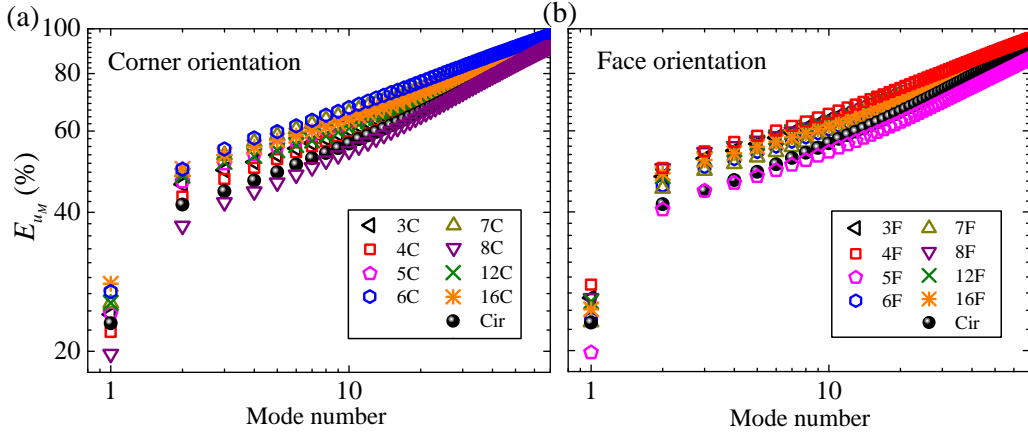

FIGURE 9 Percentage of the cumulative POD mode energy to the total energy. Mode 0, viz. the mean flow field, is excluded.

Figure 9 shows the cumulative percentage (proportion) of the mode energy E_{u_M} based on the fluctuating velocities (both u' and v') which is calculated according to the sorted eigenvalues λ_n:

$$E_{u_M} = \lambda_n / \sum_{n=1}^{N_s} \lambda_n \times 100\% \tag{7}$$

Evidently, the first two modes take $\gtrsim 40\%$ of the total fluctuating (or turbulence kinetic) energy for all the cylinders. In particular, the energy summation of the first two modes of 6C is the largest among corner orientation cases, about 50% and 8C is the least, about 37.5%. Since the first two modes mainly represent the asymmetric Karman vortex shedding process (Feng, Wang & Pan 2011; Shi & Feng 2015), it indicates that the vortex shedding process of 6C case is the most energetic, which is in agreement with the distribution of $\overline{u'u'}/U_\infty^2$ in figure 6 and $\overline{v'v'}/U_\infty^2$ in figure 7, bearing in mind that POD takes into account the entire FOV, viz. $0.7D \lesssim x \lesssim 8D$. For face orientation, the distribution of modal energy is less scattered, with 4F having the largest summation of the energy from the first two modes of 49.5% and 5F the least about 40%, also in consistent
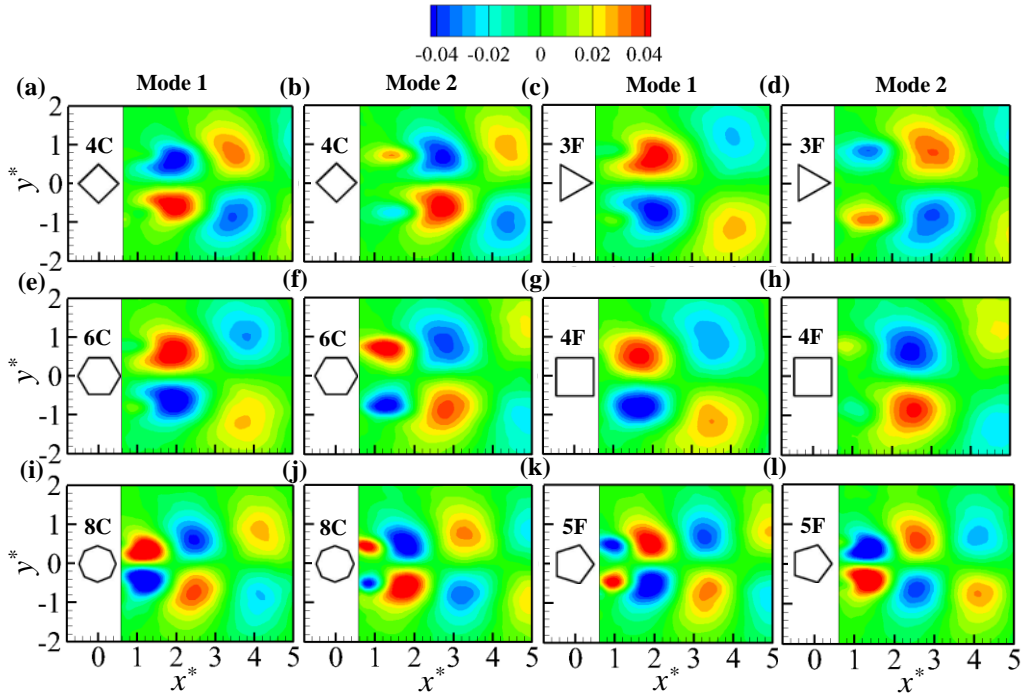
with the Reynolds stresses.

FIGURE 10 The first and second POD modes of polygonal cylinders. Contours are based on u' only.

The first two POD modes of u' are shown in figure 10 to visualize their coherent structures related to the vortex shedding patterns, using the special cases discussed in section 3.1. The first two modes display an antisymmetric pattern, which represents the alternative vortex shedding process. The patterns of the first and second modes are similar, despite a about 1/4 wavelength λ advection in the streamwise direction when +/- signs are neglected, with the wavelength meaning the streamwise distance between two successive packets of the same sign at one side of the centerline within one mode. On the one hand, the downstream distance of the first antisymmetric packet pair in mode 1 has a qualitative indication of the vortex formation length, which means 8C and 5F has shorter formation length compared to other cases. On the other hand, the size of the first packet pair is qualitatively proportional to the peak circulation of the shed vortices, which will be quantified later.

The distance between the first pair in the transverse direction in mode 1 is related to the wake width. The cases 8C and 5F have smaller wake width, which is consistent with the discussion in section 3.1. The streamwise development of this distance can be used for an estimation of the wake width growth rate. It must be emphasized that the centroids of

these packets shown in figure 10 are not the centroids of the vortices shed from the cylinders, which is investigated next.

3.3. *Evolution of vortex structures*

3.3.1 *Vortex detection and quantification method*

Due to the relatively high *Re*, instantaneous vortices appear distorted and fragmented, as shown in figure 11(a), especially in the wind tunnel experiments, which increases the difficulty in identifying their centers. This problem is tackled as follows. Firstly, for each instantaneous snapshot, the spanwise vorticity ω_{raw} field is reconstructed based on the first few energetic POD modes such that the reconstructed voriticity ω_{rd} field contains 95% of the total energy in the ω_{raw} field. Here subscripts *raw* and *rd* stand for the PIV-measured raw data and the POD reduced order reconstruction, respectively. The number of snapshots *n* required to achieve this percentage varies from one case to another, but for most cases $n = 3$. As such, the vortices appear better defined, as illustrated in figure 11(b). Secondly, to discriminate the rollup shear layers, which may contaminate the detection of vortices, from the ω_{rd} data (see the most upstream two vorticies in figure 11b as examples), the λ_{ci} method proposed by Zhou *et al.* (1999) is applied, where λ_{ci} is the imaginary part of the complex eigenvalue of the POD-reconstructed velocity gradient tensor. The λ_{ci} provides a measure for the swirl strength to allow shear layers to be excluded from detections, as illustrated in figure 11(c), where a low level threshold of $\lambda_{ci}D/U_\infty = 0.13$ ($\lambda_{ci} = 50\text{s}^{-1}$) is applied to the snapshot. Thirdly, a standard watershed segmentation algorithm is applied on the λ_{ci} fields to identify the boundary of each vortex (figure 11d). Following Sung & Yoo (2003), we can then determine the vortex center (x_c, y_c) by the λ_{ci}-weighted centroid. Symbol ★ in figure 11(a) illustrates the identified centroid or the 'center of swirl'. The results appear to be reasonable.
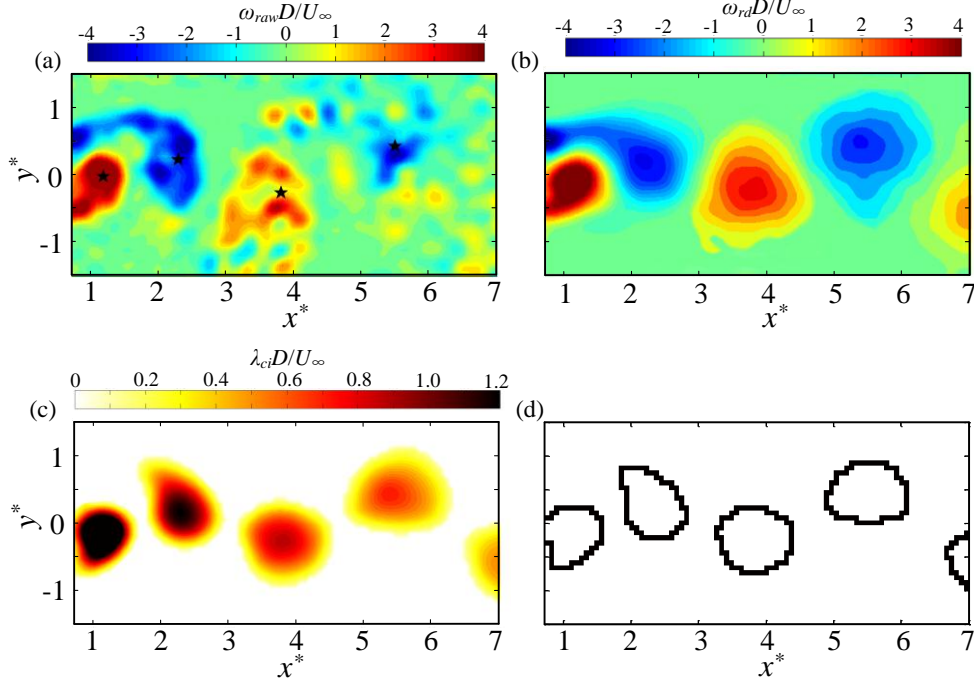
FIGURE 11. Procedure of centroid determination for individual vortices, where case 5F is used as an example. (a) Instantaneous raw vorticity (ω_{raw}) field; (b) corresponding reduced order reconstructed vorticity (ω_{rd}) field; (c) λ_{ci}-contours; (d) identified vortex boundaries.

The mean vortex strength, which is quantified by the circulation Γ, can be calculated from a conditional averaging process. In particular, the ω_{raw} distribution along the streamwise and lateral directions, $r(x)$ and $r(y)$, centered at each (x_c, y_c) are conditionally averaged based on the x_c values. A bin size of $\pm 0.1D$ is used to ensure a good sample size at each station, which is typically between $70 \sim 80$. The sample size is found to be similar at all stations, reassuring that the current PIV sampling rate is not locked at a certain phase of the wake during measurements. Figure 12(a) presents the wake behind 5F to illustrate the result of conditional averaging when x_c of a negative-sensed vortex is found in the bin centered at $x = 2.5D$. The two (x_c, y_c) trajectories of vortex centroid, obtained from the conditional averaging of individual centroids, are also presented together with the wake half width $\delta_{1/2}$ as reference, which is the vertical distance between the two points where the mean streamwise velocity falls to half of the maximum deficit.
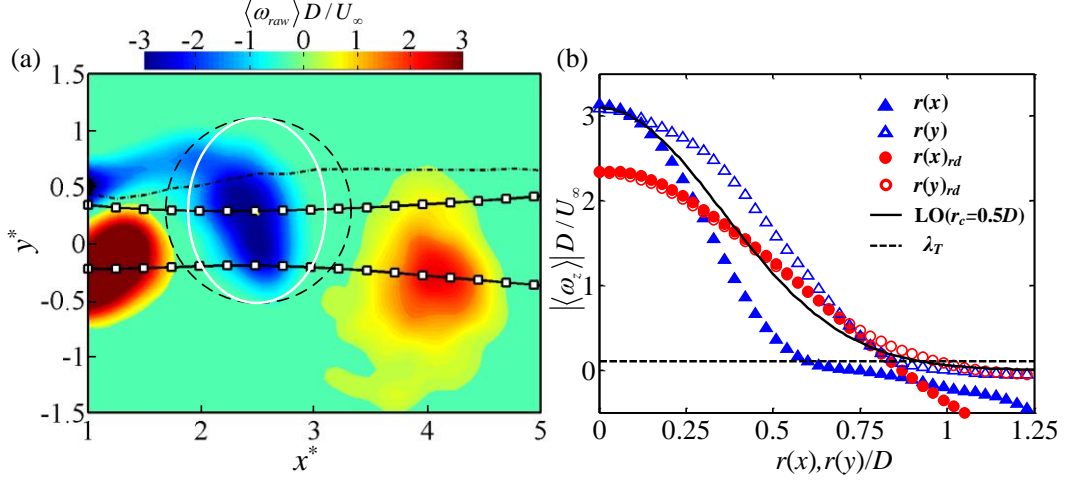
FIGURE 12. Estimation of circulation for the vortex at $x = 2.5D$ behind the 5F case. (a) The conditional averaged raw vorticity field, -□-, the trajectory of the detected vortex centroid (x_c, y_c), -·- the wake half width $\delta_{1/2}$; (b) the conditional averaged $\langle \omega_z \rangle$ profiles in both streamwise $r(x)$ and lateral $r(y)$ directions.

Figure 12(b) shows the conditional averaged vorticity $\langle \omega_z \rangle$ profiles based on ω_{raw} and ω_{rd}, respectively. A number of observations can be made. Firstly, the reduced order reconstruction yields a less pronounced vorticity peak, which is not surprising. It is for this reason that the subsequent Γ calculation is based on ω_{raw} rather than ω_{rd}. It can also be inferred that the shape of the vorticity distribution based on ω_{raw} is different from that based on ω_{rd}. Secondly, a threshold λ_T, set at $|\langle \omega_z \rangle| D / U_\infty = 0.1$, is applied when calculating Γ for all the vortices detected, where $\langle \omega_z \rangle$ denotes the conditional averaged vorticity. The intersections of λ_T with $\langle \omega_z(x) \rangle$ and $\langle \omega_z(y) \rangle$, denoted as r_x and r_y respectively, set the two principal radii of an ellipse (the white solid line in figure 12a). The circulation Γ can then be estimated as:

$$\Gamma(\lambda_T) = \oint_L \boldsymbol{u} \cdot d\boldsymbol{l} = \pi \left[\int_0^{r_x} x \langle \omega_z(x) \rangle dx + \int_0^{r_y} y \langle \omega_z(y) \rangle dy \right], \tag{8}$$

where the path L is the boundary of the ellipse. Thirdly, Zhou & Antonia (1993) used a Lamb-Oseen (LO) vortex model to describe the vorticity distribution of vortices in a circular cylinder wake, which is examined presently. The LO vorticity distribution, equation (9), is found to be between the $\langle \omega_z(x) \rangle$ and $\langle \omega_z(y) \rangle$ distributions based on ω_{raw} in figure 12(b).

$$\langle \omega_z \rangle = \langle \omega_{zp} \rangle EXP(-r^2 / r_c^2), \tag{9}$$

17

where $\langle\omega_{zp}\rangle$ is the local peak $\langle\omega_z\rangle$ and r_c is the characteristic core radius. Γ for the LO model can be readily integrated as

$$\Gamma(\text{LO}) = \pi r_c^2 \langle\omega_{zp}\rangle \left[1 - EXP(-r_T^2 / r_c^2)\right], \tag{10}$$

where r_T (the dashed line in figure 12a) is determined by λ_T. It seems plausible from figure 12(b) that equation (8), based on the model of elliptical vortex shape, may provide a more reasonable estimate for vortex strength than the LO model or equation (10). For comparison, another method to estimate Γ based on λ_{ci} is proposed below,

$$\Gamma(\lambda_{ci}) = \int_B \omega_{raw}(x, y) dB, \tag{11}$$

where area B is enclosed by the contour of $\lambda_{ci} = 50\text{s}^{-1}$ (figure 11c).

Figure 13(a) compares the downstream variations in Γ calculated from equation (8) with $\langle\omega_z\rangle$ based on ω_{raw} and ω_{rd}, respectively, denoted as λ_T and $\lambda_{T,rd}$, and equations (10) (based on $\omega_{raw}(y)$) and (11), denoted as LO and λ_{ci}. The downstream variation in the equivalent diameter D_t is shown in figure 13(b), where $D_t = r_x + r_y$ for the elliptical model, $r_x = r_y = r_T$ for the LO model, and $D_t = \sqrt{4B/\pi}$ for the λ_{ci} method. Figure 13(c) shows the aspect ratio r_x/r_y and the centroid scattering ratio $\sigma_{y_c}/\sigma_{x_c}$, where σ_{x_c} and σ_{y_c} denote the standard deviation of x_c and y_c from the conditional averaging process, respectively. The fact that $\sigma_{y_c} < \sigma_{x_c}$ for the entire range is ascribed to the finite bin size in the x direction during conditional averaging.

It is evident in figure 13(a) that $\Gamma(\lambda_T)$ and $\Gamma(\lambda_{ci})$ agree reasonably well with each other. The former is consistently larger because of a relatively high threshold set for λ_{ci} to minimize erroneous detections. Both $\Gamma(\lambda_T)$ and $\Gamma(\lambda_{ci})$ decrease with x, which is expected. On the other hand, D_t changes little, when estimated from the λ_{ci} method, but increases slowly when estimated by the λ_T method (figure 13b). The increase in D_t captured by the λ_T method is consistent with our perception of downstream vorticity diffusion, thus suggesting a superiority, in this respect, to the λ_{ci} method.
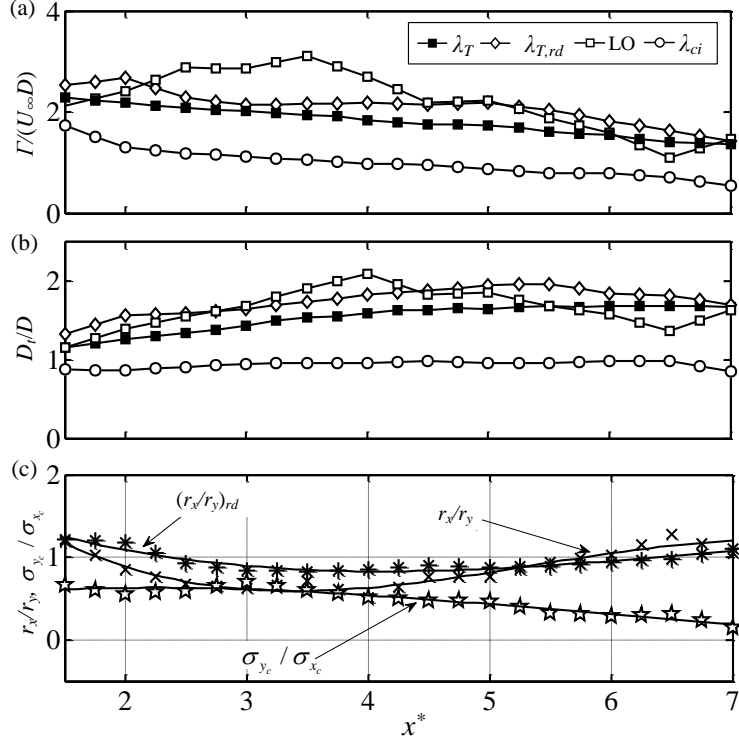
FIGURE 13. Downstream evolution of vortices for case 5F. (a) Comparison of circulation calculated by equations (8), (10) and (11); (b) equivalent vortex diameter D_t; (c) ratios r_x/r_y and $\sigma_{y_c}/\sigma_{x_c}$ where solid lines are polynomial fits to the raw data.

The predicted Γ from the LO model tends to exceed those from other methods and its downstream variation exhibits appreciable difference from others (figure 13a). The observation is attributed to the unreasonable circular model of the LO method. This can be inferred from r_x/r_y in figure 13(c). The excess range of Γ, compared to $\Gamma(\lambda_T)$ and $\Gamma(\lambda_{ci})$, coincides with the range of $r_x < r_y$ which indicates a vortex elongation along the y direction (cf. figure 12a). The result implies that the LO model may result in an overestimate of Γ. The POD-reconstructed $\Gamma(\lambda_{T,rd})$ is consistently larger than $\Gamma(\lambda_T)$ because some areas of low vorticity are embraced as part of the coherent structure, as confirmed by the larger D_t (figure 13b). The conditionally averaged vortex structure from the POD reconstruction displays a more circular shape throughout the measured x range. That is, the $(r_x/r_y)_{rd}$ is closer to unity (figure 13c). As a result, the lateral elongation of actual vortices may have been under-represented in the POD-reconstructed model. In conclusion, $\Gamma(\lambda_T)$ is considered to provide a better surrogate for the true Γ.

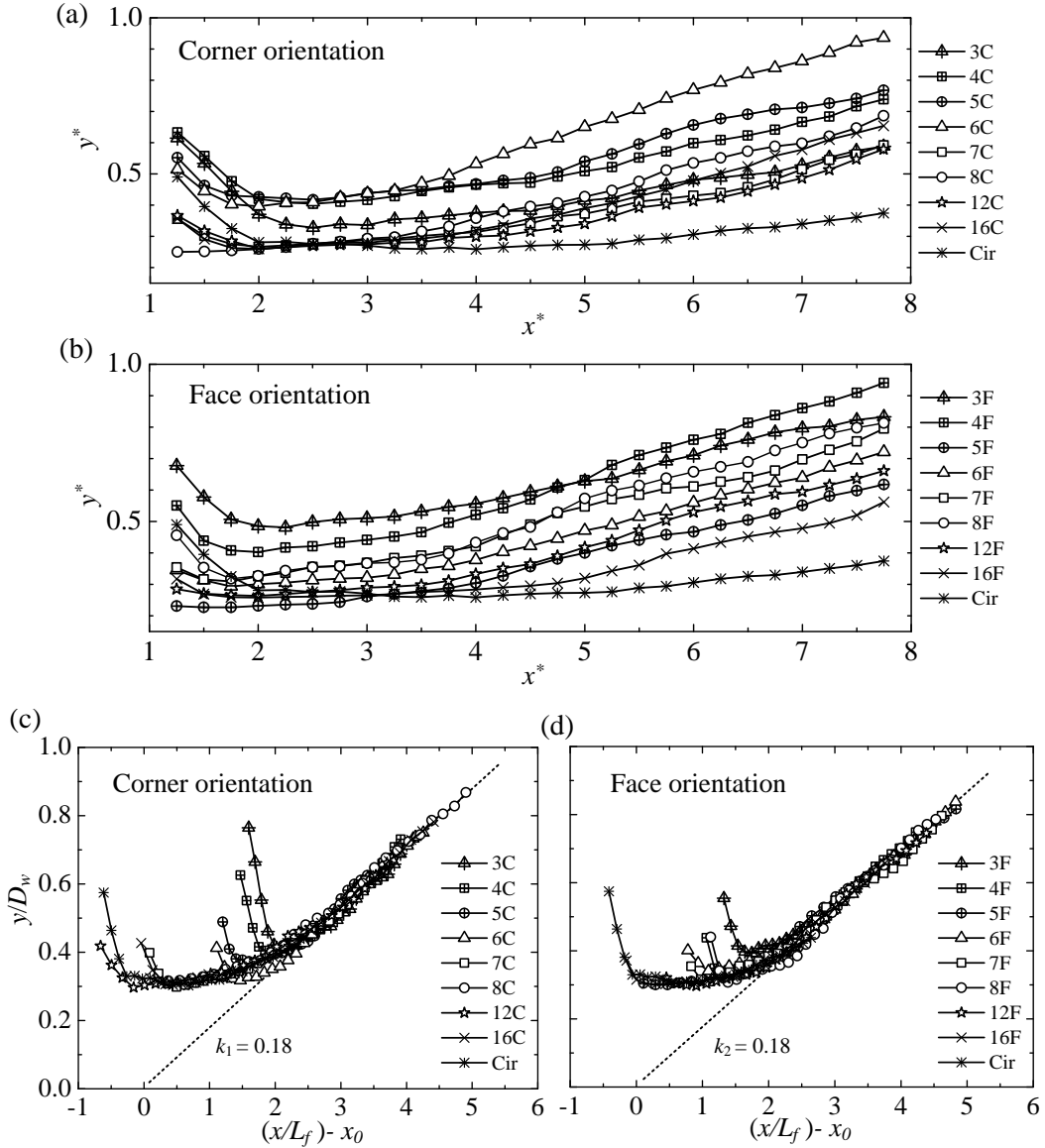### 3.3.2 *Strength, size and path of spanwise vortices*

FIGURE 14. Trajectories of vortex centers: (a), (b) x and y scaled by D; (c), (d) x and y scaled by L_f and D_w, respectively, where the abscissa is shifted by the virtual origin x_0.

The trajectories of the conditionally averaged vortex centroid (x_c, y_c) are presented in figure 14(a, b) for various polygonal cylinders. In general, y_c decreases first to a minimum during the vortex formation process and then increases gradually. A similar observation was reported in Kim, Yoo & Sung (2006) and Shi & Feng (2015) for the circular cylinder wake. The minimum y_c occurs at $x \approx L_f$ for $N \leq 8$, but consistently at a downstream position beyond L_f for $N > 8$. As L_f and D_w are the characteristic length scales related to the vortex formation, it is physically meaningful to re-scale the ordinate and the abscissa

by D_w and L_f, respectively. Furthermore, the origin of the abscissa is shifted to the virtual origin, x_0, which is the intersection point between the asymptotic straight line of the vortex center trajectory and the abscissa in the far field. As shown in figure 14(c, d), y_c/D_w declines initially and the scaled rate $(dy/D_w)/(dx/L_f)$ (negative) is similar for all cases, regardless of N and the orientation. Further downstream, y_c/D_w increases, the trajectories collapse together on the curve $y/D_w = 0.18(x/L_f - x_0)$ whose slope $k_1 = k_2 \approx 0.18$. That is, the ratio of the scaled lateral to streamwise components of the vortex convection velocity approaches 0.18 asymptotically after the vortex formation.
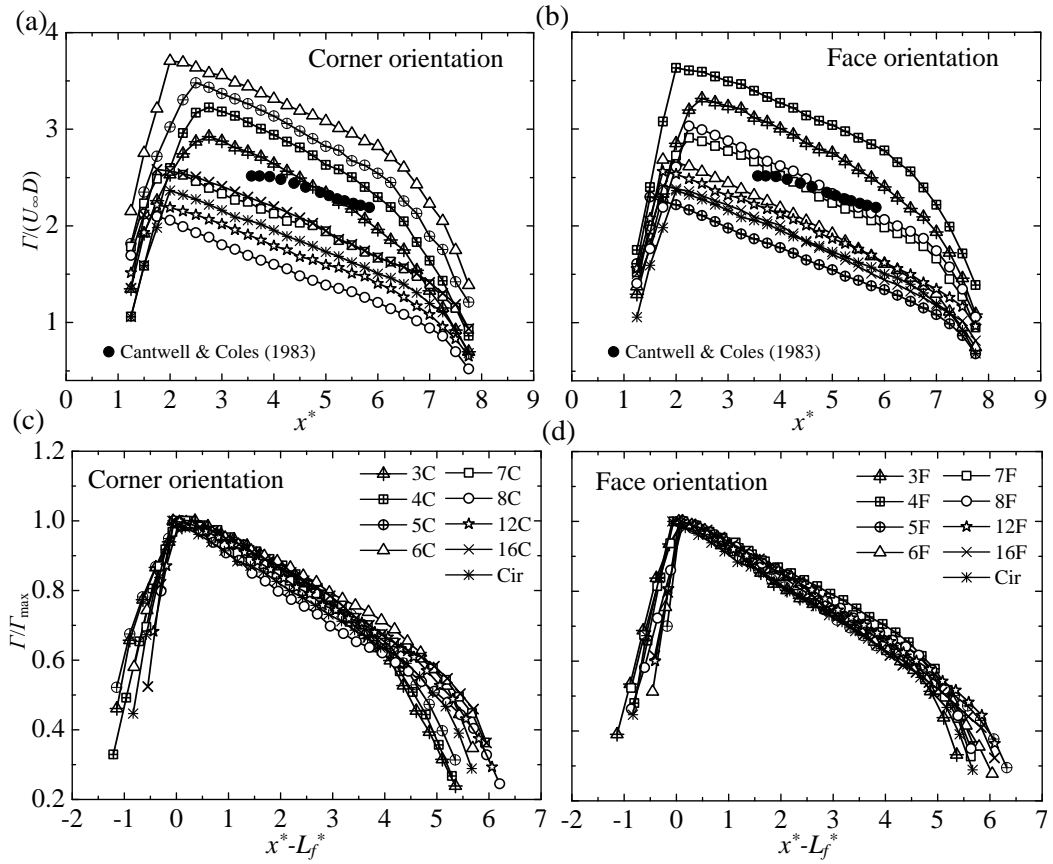

FIGURE 15. The evolution of $\Gamma(\lambda_T)$: (a), (b) raw data scaled by the constant $U_\infty D$; (c), (d) $\Gamma(\lambda_T)$ scaled by the maximum value $\Gamma(\lambda_T)_{max}$, the abscissa is shifted by the formation length L_f^*.

The evolution of the vortex strength $\Gamma(\lambda_T)$ on x^* is similar for all cylinders (figure 15a, b). At the early stage, $\Gamma(\lambda_T)$ rises rapidly until reaching its maximum at $x \approx L_f$. This initial development corresponds to the shear layer rollup process, during which the vorticity in the shear layer is continuously entrained into the leading vortex; see figure 15(a). For instance, cases 8C and 5F reach the maximum $\Gamma(\lambda_T)$ at the smallest x^*, that is, their L_f^* is

smallest, which is consistent with figure 2(a). After that, the vortices quickly detach from the shear layer and are convected downstream at a velocity in the order of U_∞, forming the Karman vortex street, At the same time, $\Gamma(\lambda_T)$ decays under the combined effect of viscous dissipation and cancellation between opposite sensed vortices (figure 15a, b). The decay rate of Γ in the circular cylinder wake agrees qualitatively well with Cantwell & Coles' (1983) observation at $Re = 1.4 \times 10^5$. Their measured Γ is appreciably larger than the present estimate for the circular cylinder wake. The magnitude of Γ and its decay rate are influenced by the threshold levels set to define the vortex boundary, which was $\left| \langle \omega_z \rangle \right| D / U_\infty = 0.03$ in Cantwell & Coles (1983) but 0.10 presently. Therefore, the difference between the two studies is not unexpected.

Figure 15(c, d) shows $\Gamma(\lambda_T)$, normalized by its maximum Γ_{max}, against $x^* - L_f^*$, which displays a reasonably good collapse, irrespective of N and the cylinder orientation. Several common features may be extracted from the collapsed data. Firstly, the vortex reaches its maximum strength at the formation length $x \approx L_f$. Secondly, the vortex exhibits two stages of decay after reaching its maximum. The first stage is an almost linear decay, which extends to slightly beyond $4D$ and near $5D$ behind L_f for the corner and face orientations, respectively. The slopes of the linear decay are very close to each other for all the cases, that is, the decay rate is almost independent of N and the orientation. It might imply a decay process mainly driven by the vorticity diffusion and dissipation, also reflected by the decline of the peak vorticity at the vortex center. Further downstream, the decay rate becomes appreciably larger and is more sensitive to N. It is possibly owing to the combined effects of vorticity diffusion, dissipation and vigorous interactions and cancellation between neighboring vortices which grow to a significant size. More discussion on the latter point will be given later. To the authors' best knowledge, the two-stage decay in the vortex strength and their turning point have not been reported previously. Finally, the fact that $\Gamma(\lambda_T)_{max}$ occurs at L_f^* suggests that L_f is a suitable scaling factor for the streamwise length scale in the near wake.
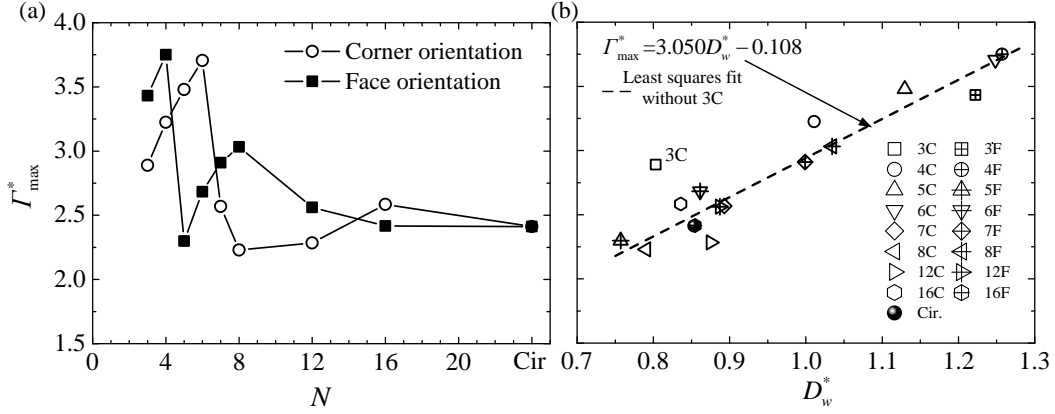
FIGURE 16. Dependence of Γ^*_{max} on (a) N and (b) D_w^*. The dashed line in figure (b) is the straight line least-square-fitted to the data of all polygonal cylinders, excluding the 3C case.

$\Gamma^*_{max}(=\Gamma_{max}/(U_\infty D))$ depends on N and the cylinder orientation, as shown in figure 16(a). It can be found that 6C and 4F cases has the maximum vortex circulation in the wake for corner and face orientation respectively, 8C and 5F cases are the opposite, which is consistent with the analysis of the Reynolds normal stress (figure 6) and POD mode energy (figure 9). Figure 2(b) indicates that D_w^* distribution with N is similar with Γ^*_{max} distribution; this prompts us to plot Γ^*_{max} against D_w^*, as shown in figure 16(b). Interestingly, Γ^*_{max} and D_w^* of the polygonal cylinders are indeed correlated linearly, except 3C case that are characterized by the largest flat leeward surface (lack of aft-body). The result points out that the maximum circulation of the vortices should scale with U_∞ and D_w^*.

While the vortices decay in their strength downstream, their size grows due to vorticity diffusion. The characteristic size of the vortices may be represented by D_t. Although dependent on N and the cylinder orientation, D_t increases monotonically over the streamwise range examined (figure 17a, b). Furthermore, its growth rate is similar, albeit dropping slowly as x increases. Use D_{t0} to denote D_t at $\Gamma(\lambda_T)_{max}$ (figures 15a, b and 17a, b) and shift the ordinate by D_{t0}^*, as shown in figure 17(c, d). Since $\Gamma(\lambda_T)_{max}$ occurs at L_f^* (figure 15c, d), the abscissa in figure 17(c, d) is shifted by L_f^* accordingly. We see immediately that the evolution of D_t is approximately the same for all N and the two orientations. The data scattering is more appreciable at $x > 2L_f$, especially with the corner orientation, and the cylinders of smaller N, i.e. 3C~6C for the corner orientation and

3F~4F for the face orientation, are associated with smaller growth rate of D_t. For $x < L_f$, the growth of D_t is owing to the entrainment of shear layer vortices and, as is evident in figure 15(c, d), this effect is essentially the same for all cases, as is expected.
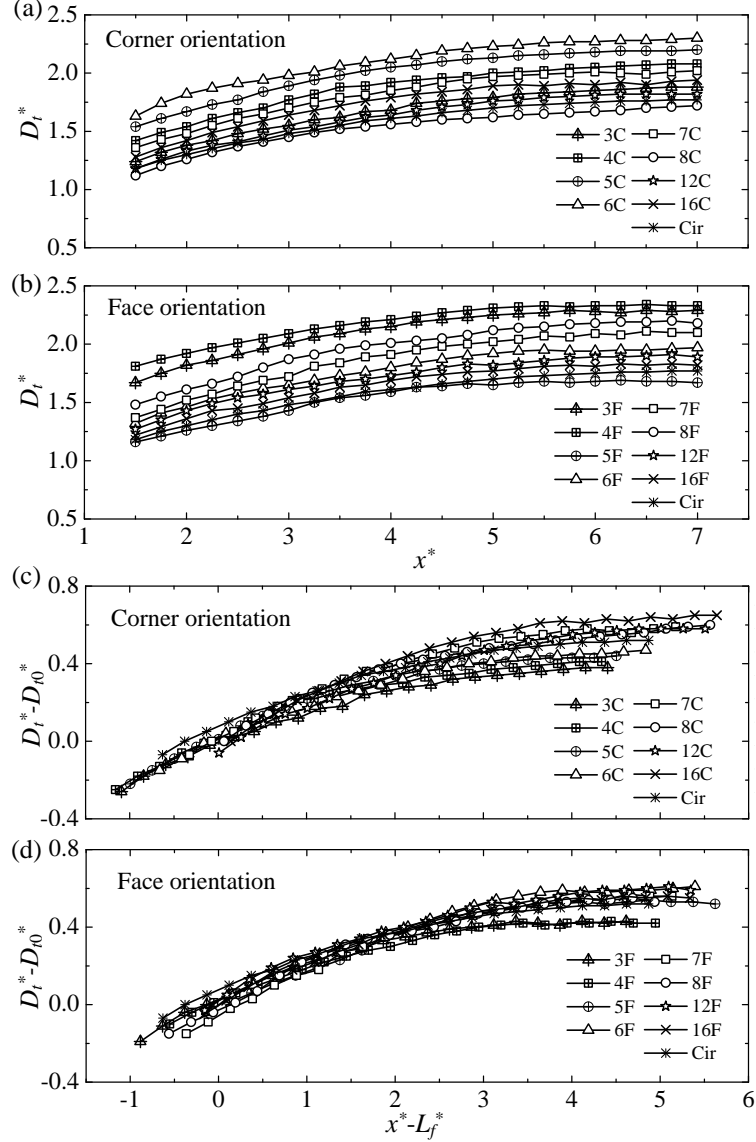

FIGURE 17. The evolution of the equivalent vortex diameter D_t. (a), (b) D_t/D (D_t^*); (c), (d) the ordinate and the abscissa are shifted by D_{t0}^* and L_f^*, respectively.

Figure 18(a, b) presents the dependence of D_{t0}^* on N and D_w^*, respectively. The latter points out unequivocally that D_{t0}^* is linearly related with D_w^*, which is fully consistent with the conception that the characteristic width of the wake is linked to the vortex size. At the location where the circulation reaches its maximum, the vortex size D_{t0} $\approx 1.6 D_w$ when the threshold is set at $|\langle\omega_z\rangle|D/U_\infty = 0.1$. Case 3C is the exception, which is similar with Γ_{max}^* vs. D_w^* in figure 16(b).

The deviation of 3C could be explained as follows. The flow separation points for 3C occurs at the most rear position compared to the other cases, according to the flow visualization in Xu et al (2017). This results in a very small D_w^* amongst all the cases as shown in figure 2. Furthermore, because of the location of the separation points, the 3C case lacks of an aft-body, which minimizes the effect of the cylinder body on the vortex formation process.
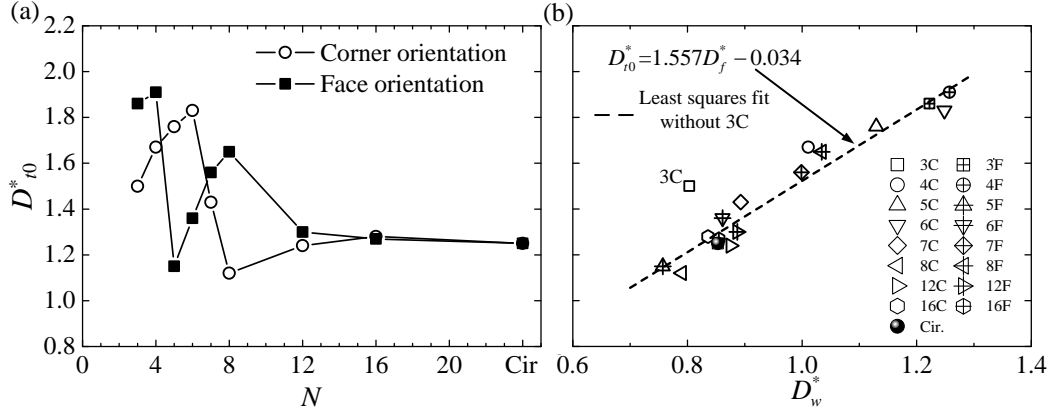

FIGURE 18. Dependence of D_{t0}^* on (a) N and (b) D_w^*. The dashed line in figure (b) is the straight line least-square-fitted to the data of all polygonal cylinders, excluding the 3C case.

3.3.3 Convection velocity of vortices

In this section, we present the dependence on N of the convection velocity of vortices in the wake, which is a fundamentally important quantity, especially in the framework of Taylor's hypothesis adopted widely for the spatiotemporal correlations of turbulent flows to explain entrainment and transport processes in the frame of reference translating with vortices (Cantwell & Coles 1983). Zhou & Antonia (1992) compared different methods to quantify vortex convection velocities in the wake of a circular cylinder for the range $10 \leq x/D \leq 60$, where the convection velocity was estimated by the velocity at the vortex center. Theoretically, the averaged vortex convection velocity $\{U_c, V_c\}$ equal the conditional averaged velocity on the vortex centroid (x_c, y_c) because Helmholtz first law states that the vortex lines move with the fluid, that is, a shed vortex is swept downstream at the local velocity at the vortex center. On the other hand, since an isolated vortex induces zero velocity at its own center, the detected velocity there will be the linear combination of the background velocity and the velocity induced by other vortices in the street at that

particular phase. The local vortex is then convected at this resultant velocity.
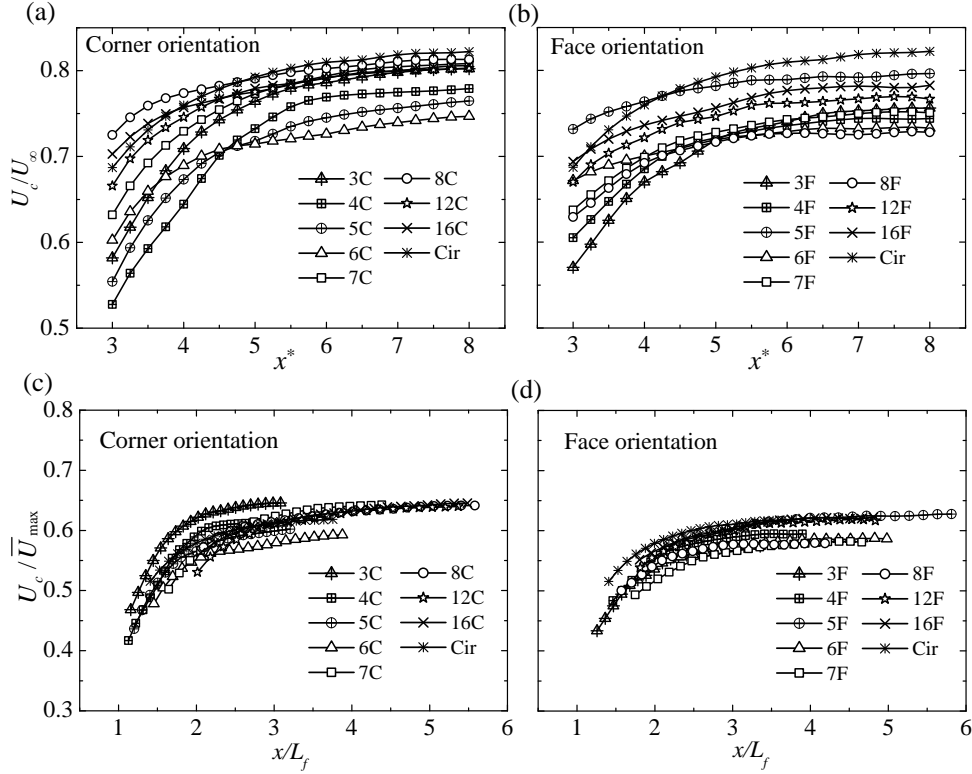

FIGURE 19. (a), (b) The variation of the streamwise vortex convection velocity U_c for all cylinders, (c), (d) The variation of the scaled U_c by $\bar{U}_{\max}$, the abscissa is rescaled by L_f.

The variation in U_c with x is given in figure 19(a, b) over $3 \leq x/D \leq 8$, over which the vortices are completely detached from the shear layer under the influence of the convective instability. Apparently, $U_c < U_\infty$, though they are in the same order of magnitude. One observation can be made, that is, U_c increases monotonically, with a gradually reducing dU_c/dx, irrespective of N and the cylinder orientation. The result conforms to previous reports on U_c for $N = \infty$ (Cantwell & Coles 1983) and the 4F case (Hu, Zhou & Dalton 2006). In the near field, U_c is largely related to the local velocity deficit, which is strongly dependent on N and the orientation. Cases 4C and 3F are associated with the lowest U_c, while 8C and 5F with the largest. This is internally consistent with the larger velocity deficit for the cases of 4C and 3F and smaller velocity deficit for the cases of 8C and 5F for the same x^* range (figure 3). On the other hand, cases 4C and 3F correspond to the largest dU_c/dx, while 8C and 5F to the smallest. Further downstream, the velocity deficit shrinks and U_c recovers. Near the end of FOV, U_c rises to

$(0.72\sim0.82)U_\infty$, with the largest U_c in the circular cylinder wake; its dependence on N and the orientation becomes weaker.

With U_c and x normalized by $\overline{U}_{max}$ (the maximum mean streamwise velocity value near the cylinder in the wake) and L_f, respectively, the scattering in the normalized U_c is greatly reduced, as shown in figure 19(c, d). This allows us to extract one common feature of U_c for all the cases, that is, the variation rate of U_c exhibits a clear change at $x \approx 2L_f$, which correspond two stages of convection velocity evolution. At $x < 2L_f$, $U_c/\overline{U}_{max}$ increases dramatically because of the quick recovery of the velocity deficit in the near wake. At $x > 2L_f$, $U_c/\overline{U}_{max}$ keeps a constant value basically, because the mean streamwise velocity increases very slowly in the wake. It is also noticeable that the 3C case differs most in $U_c/\overline{U}_{max}$ from the other cases, which is attributed to its large Γ^*_{max} (figure 16b).

4. Conclusions

The wakes behind various polygonal cylinders are systematically studied at subcritical regime, $Re = 1.6\times10^4$. The side number N of the polygonal cylinder is 3 to 16, along with $N = \infty$ (a circular cylinder) which acts as a reference for comparison. ~~Two orientations are investigated for each cylinder: the corner or flat surface facing incoming flow.~~ The dependence on N and the cylinder orientation of the mean velocity, the Reynolds stresses, and the coherent structures of the near wake are examined carefully. Vortices in the wake are extracted from POD and phase averaging and are characterized in terms of their strength, path, size and convection velocity. ~~Some conclusions can be drawn below.~~

(1) The near-wakes of the polygonal cylinders exhibit a significant dependence on N and the cylinder orientation, as reflected by the mean velocity profiles, Reynolds stress distributions and the vortex formation length L_f and wake width D_w. Cases 8C and 5F show the smallest L_f, D_w and lowest Reynolds stress magnitude, with the smallest velocity deficit and fastest velocity recovery in the near wake. ~~It is believed to relate to the smallest circulation Γ of the shed vortices behind these cylinders. That is, 8C and 5F have the smallest Γ and the fastest Γ saturation among the cylinders in the two orientations (figure 13a, b), resulting in the shortest vortex formation and weakest~~

(2) The vortex circulation grows to the maximum at the vortex formation length ($x \approx L_f$) and then decays downstream. The decay may be divided into two stages. The first stage, up to $5L_f^*$, is characterized by a linear decay rate almost independent of N and orientation, and is probably dominated by vorticity diffusion and viscous dissipation. The second stage, beyond $5L_f^*$, is featured with a faster decay rate, which differs from one cylinder to another, probably resulting from the combined effect of diffusion, dissipation and vigorous vortex interactions. To our best knowledge, the two stage decay in the vortex strength and their turning point at $x^* \approx 5L_f^*$ have not been reported previously. The maximum vortex strength Γ_{max}^* in the wake is found to be linearly related to D_w^* (figure 16b).

(3) The conditionally averaged vortex path indicates that the vortices move towards the centerline first and then away. In the normalized coordinate system (x/L_f, y/D_w), the ratio of the lateral and streamwise components of the vortex convection velocity is fixed at $(dy/D_w)/(dx/L_f) \approx 0.18$ (as $dy/dx = V_c/U_c$) for $x > 2L_f$, irrespective of the cylinder orientation and N. The equivalent diameter, D_t, of vortices grows monotonically downstream for all cylinders. While D_t is clearly dependent on N and the cylinder orientation, its growth rate scaled by L_f is approximately the same for all the cases (figure 17c, d). D_t^* corresponding to $\Gamma(\lambda_T)_{max}$ is linearly correlated with D_w^* (figure 18b). which is fully consistent with the conception that the characteristic width of the wake is linked to the vortex size. The streamwise component U_c of the vortex convection velocity, scaled by $\bar{U}_{max}$, displays two distinct growth rates, separated at $x \approx 2L_f$. U_c is influenced by the background averaged velocity. As inferred from figure 3, the streamwise averaged velocity recovers rapidly for $x < 2L_f$ in the near wake, contributing to the high growth rate of U_c and then approaches to a constant for $x > 2L_f$. accounting for the lower growth rate.

REFERENCES

AGRWAL, N., DUTTA, S. & GANDHI, B. K. 2016 Experimental investigation of flow field behind triangular prisms at intermediate Reynolds number with different apex angles. *Exp. Therm. Fluid Sci*. **72**, 97-111.

ALAM, M. M., ZHOU, Y. & WANG, X. W. 2011 The wake of two side-by-side square cylinders. *J. Fluid Mech*. **669**, 432–471.

APELT, C. J., WEST, G. S., & SZEWCZYK, A. A. 1973 The effects of wake splitter plates on the flow past a circular cylinder in the range $10^4 < R < 5 \times 10^4$. *J. Fluid Mech*. **61**(1), 187-198.

BAI, H. L., ALAM, M. M., GAO, N. & LIN, Y. F. 2019 The near wake of sinusoidal wavy cylinders: three-dimensional POD analyses. *Int. J. Heat Fluid Fl*. **75**, 256-277.

BEARMAN, P. W. 1969 On vortex shedding from a circular cylinder in the critical Reynolds number regime. *J. Fluid Mech*. **37**.3: 577-585.

BERKOOZ, G., HOLMES, P. & LUMLEY, J. L. 1993 The proper orthogonal decomposition in the analysis of turbulent flows. *Annu. Rev. Fluid Mech*. **25**:539-575.

BLOOR, M. S. 1964 The transition to turbulence in the wake of a circular cylinder. *J. Fluid Mech*. **19**, 290–304.

CANTWELL, B. & COLES, D. 1983 An experimental study of entrainment and transport in the turbulent near wake of a circular cylinder. *J. Fluid Mech*. **136**, 321-374.

CHATTERJEE, A. 2000 An introduction to the proper orthogonal decomposition. *Curr. Sci*. **78**, 808-817.

CHOPRA, G. & MITTAL, S. 2019 Drag coefficient and formation length at the onset of vortex shedding. *Phys. Fluids* **31**.1: 013601.

FENG, L. H., WANG, J. J. & PAN, C 2011 Proper orthogonal decomposition analysis of vortex dynamics of a circular cylinder under synthetic jet control. *Phys. Fluids* **23**, 014-106.

GRIFFIN, O. M. 1995 A note on bluff-body vortex formation. *J. Fluid Mech.* **284**, 217-224.

HE, G. S., LI, N. & WANG, J. J. 2014 Drag reduction of square cylinders with cut-corners at the front edges. *Exp. Fluids* **55**(6), 1745.

HU, J. C., ZHOU, Y. & DALTON, C. 2006 Effects of the corner radius on the near wake of a square prism. *Exp. Fluids* **40**, 106-118.

KAFFEL, A., MOUREH, J., HARION, J. L. & RUSSEIL, S. 2016 TR-PIV measurements and POD analysis of the plane wall jet subjected to lateral perturbation. *Exp. Therm. Fluid Sci.* **77**: 71-90.

KHALEDI, H. A. & ANDERSSON, H. I. 2011 On vortex shedding from a hexagonal cylinder. *Phys. Lett. A* **375**(45), 4007-4021.

KIM, W., YOO, J. Y. & SUNG, J. 2006 Dynamics of vortex lock-on in a perturbed cylinder wake. *Phys. Fluids* **18**, 074-103.

KIM, Y. C., BANDI, E.K., YOSHIDA, A., & TAMURA, Y. 2015 Response characteristics of super-tall buildings - Effects of number of sides and helical angle. *J. Wind Engng Ind. Aerodyn.* **145**, 252-262.

LIN, J. C., TOWFIGHI, J. & ROCKWELL, D. 1995 Instantaneous structure of the near-wake of a circular cylinder: on the effect of Reynolds number. *J. Fluids Struct.* **9**.4: 409-418.

LYN, D. A., EINAV, S., RODI, W. & PARK, J. H. 1995 A laser-Doppler velocimetry study of ensemble-averaged characteristics of the turbulent near wake of a square cylinder. *J. Fluid Mech.* **304**, 285-319.

MEYER, K. E., PEDERSEN, J. M. & OZCAN, O. 2007 A turbulent jet in crossflow analysed with proper orthogonal decomposition. *J. Fluid Mech.* **583**, 199-227.

MONKEWITZ, P. A. & NGUYEN, L. N. 1987. Absolute instability in the near-wake of two-dimensional bluff bodies. *J. Fluids Struct.* **1**(2), 165-184.

MURALIDHAR, S. D., PODVIN, B., MATHELIN, L., & FRAIGNEAU, Y. 2019 Spatio-temporal proper orthogonal decomposition of turbulent channel flow. *J. Fluid Mech.* **864**, 614-639.

NORBERG, C. 2003 Fluctuating lift on a circular cylinder: review and new measurements. *J. Fluids Struct.* **17**.1: 57-96.

PEREIRA, F. S., ECA, L., VAZ, G. & GIRIMAJI, S. S. 2019 On the simulation of the flow around a circular cylinder at *Re* = 140,000. *Int. J. Heat Fluid Fl.* **76**: 40-56.

QU, Y., WANG, J. J., SUN, M., FENG L. H., PAN, C., GAO Q. & HE, G. S. 2017 Wake vortex evolution of square cylinder with a slot synthetic jet positioned at the rear surface. *J. Fluid Mech.* **812**, 940-965.

SHI, X. D. & FENG, L. H. 2015 Control of flow around a circular cylinder by bleed near the separation points. *Exp. Fluids* **56**, (12), 214.

SIROVICH, L. 1987 Turbulence and the dynamics of coherent structures. I. Coherent structures. *Q. Appl. Math.* **45**, 561-571

SUNG, J. & YOO, J. Y. 2003 Near-wake vortex motions behind a circular cylinder at low Reynolds number. *J. Fluids Struct.* **17**, 261-274.

SZALAY Z. 1989 Drags on several polygon cylinders. *J. Wind Engng Ind. Aerodyn.* **132**(1-2): 135-143.

TANG, J. W., XIE, Y. M., FELICETTI, P., TU, J. Y. & LI, J. D. 2013 Numerical simulations of wind drags on straight and twisted polygonal buildings. *Struct. Des. Tall Spec.* **22**(1): 62-73.

TANG, S. L., DJENIDI, L., ANTONIA, R. A. & Zhou, Y. 2015 Comparison between velocity-and vorticity-based POD methods in a turbulent wake. *Exp. Fluids* **56**(8), 169.

UNAL, M. F. & ROCKWELL, D. 1988 On vortex formation from a cylinder. part 1. the initial instability. *J. Fluid Mech.* **190**(1), 491-512.

VICKERY, B. J. 1966 Fluctuating lift and drag on a long cylinder of square cross-section in a smooth and in a turbulent stream. *J. Fluid Mech.* **25** (3), 481-494.

WYGNANSKI, I., CHAMPAGNE, F., & MARASLI, B. 1986 On the large-scale structures in two-dimensional, small-deficit, turbulent wakes. *J. Fluid Mech.* **168**, 31-71.

XU, S. J., ZHANG, W. G., GAN, L., LI, M. G. & ZHOU, Y. 2017 Experimental study of flow around polygonal cylinders. *J. Fluid Mech.* **812**, 251-278.

ZHOU, J., ADRIAN, R. J., BALACHANDAR, S. & KENDALL, T. M. 1999 Mechanisms for generating coherent packets of hairpin vortices in channel flow. *J. Fluid Mech.* **387**,

353-396.

ZHOU, Y., & ANTONIA, R. A. 1992 Convection velocity measurements in a cylinder wake. *Exp. Fluids* **13**(1), 63-70.

ZHOU, Y. & ANTONIA, R. A. 1993 A study of turbulent vortices in the near wake of a cylinder. *J. Fluid Mech*. **253**, 643-661.

ZHOU, Y. & ANTONIA, R. A. 1994 Effect of initial conditions on vortices in a turbulent near wake. AIAA journal **32**(6), 1207-1213.

ZHOU, Y. & ANTONIA, R. A. 1995 Memory effects in a turbulent plane wake. *Exp. Fluids* **19**(2), 112-120.